Icarus 449 (2026) 116964

Contents lists available at ScienceDirect

Icarus

journal homepage: www.elsevier.com/locate/icarus

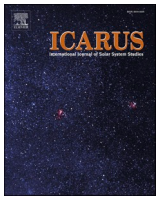

Research Paper

Validation of SPH code Spheral to model interacting solid bodies in a supersonic flow

Veronika A. Korneyeva [a,*], Jason M. Pearl [a], Kathryn M. Kumamoto [a], J. Michael Owen [a], Cody D. Raskin [a], Megan B. Syal [a], Nicholaus J. Parziale [b], Stuart J. Laurence [c]

[a] Lawrence Livermore National Laboratory, 7000 East Ave, Livermore, 94550, CA, USA
[b] Stevens Institute of Technology, 1 Castle Point Terrace, Hoboken 07030, NJ, USA
[c] University of Maryland, 4298 Campus Dr, College Park, 20742, MD, USA

ARTICLE INFO

Keywords:
Asteroids
Airburst
Planetary defense
Bow shock
Hypersonic

ABSTRACT

Contemporary discussions of planetary defense involve analyzing the risks posed by smaller sized, 20 to 200 m diameter, asteroids which are capable of breaking up in the atmosphere and generating a blast wave. Consequence assessments for this size class of asteroids are performed through fast-running analytic or semi-analytic models which are informed by high-fidelity hydrocode simulations of asteroid entry and breakup. However, insufficient historical data necessitates validating the independent physical processes which dominate airburst events. The Fluid Solid Interface Smoothed Particle Hydrodynamics solver was previously used by Pearl et al. in 2023 to model the Chelyabinsk airburst and is used here to perform a series of validation simulations. The first effort involves modeling a cylinder in a hypersonic flow and comparing the bow shock geometry to that predicted by analytic theory. The second effort involves modeling the separation of two spherical bodies in supersonic flow and validating against experimental footage. Combined, these exercises demonstrate the ability of the code to model the flight-path of interacting solid bodies in a hypersonic flow.

1. Introduction

Smaller-sized asteroids, on the order of 20 to 200 m in diameter, typically undergo rapid breakup when they enter the atmosphere in a process that transfers their kinetic energy into the surrounding air, generating a pressure driven blast wave otherwise referred to as an airburst (Hills and Goda, 1993; Brown et al., 2002; Boslough and Crawford, 2008). Depending on the velocity, size, and physical properties of the asteroid, an airburst event can either be a dazzling flash of light in the sky or substantial enough to cause structural damage and fatalities. According to Harris and Chodas (2021), the population subset of asteroids <200 m diameter is largely undiscovered (< 1%), while the subset of asteroids >1 km is mostly discovered. In addition, the orbital motion of asteroids is difficult to ascertain due to low reflectivity, high velocity, and large distances (Shao et al., 2014). The estimated quantity of sub-20-m-sized asteroids (Brown et al., 2002; Harris and Chodas, 2021) implies a relatively frequent impact interval, less than every 1000 years. The impact interval of Tunguska scale asteroids is estimated to be between every 4000 to 10,000 years (Boslough et al., 2026) however, this impact probability increases as swarms of asteroids come close to resonance with the Earth and require comprehensive surveys to determine risk. This knowledge gap in identified bodies capable of high-yield low-altitude bursts suggests the possibility of future airburst events with little to no warning time.

There are two standout cases that are regularly cited in discussions, analyses, and models of airbursts and their associated physical processes: Chelyabinsk in 2013 and Tunguska in 1908. The Chelyabinsk event was caused by an approximately 20-m asteroid which generated a blast wave that produced ground overpressures as high as 7 kPa (Brown et al., 2013) and damaged urban structures and induced sunburns, concussions and other injuries as far as 100 km from ground zero (Popova et al., 2013). The 2013 Chelyabinsk airburst event was observed globally by infrasound, seismic, USGS sensor equipment, field survey reports, and over 400 video feeds up to 700 km away (Brown et al., 2013). Subsequent research utilized this data to reconstruct the Chelyabinsk event and constrain the orbit, entry angle, velocity, trajectory, height of burst, yield, material composition, airwave arrival, and surface overpressure/radiation (Popova et al., 2013; Emelyanenko

* Corresponding author.
E-mail address: korneyeva1@llnl.gov (V.A. Korneyeva).

https://doi.org/10.1016/j.icarus.2026.116964
Received 13 August 2025; Received in revised form 13 January 2026; Accepted 19 January 2026
Available online 20 January 2026

et al., 2013; Emel'yanenko et al., 2014; Avramenko et al., 2014; Shuvalov et al., 2017; Popova, 2021). In contrast, the Tunguska event occurred nearly a century prior and was caused by an approximately 50-m asteroid which resulted in a blast wave that essentially decimated 2000-sq-km of trees in remote Siberia (Kulik, 1936). It is estimated that the Tunguska airburst released 3 to 30 Mton of energy into the atmosphere (Longo, 2007). This wide range is primarily constrained by eyewitness accounts and field surveys of the treefall performed years after the event occurred as well as by modern hydrocode simulations (Boslough and Crawford, 1997; Artemieva and Shuvalov, 2016; Jenniskens et al., 2019; Robertson and Mathias, 2019).

To better understand the hazards posed by asteroid airbursts, two different approaches have been adopted to model atmospheric breakup – ODE-based models and hydrocode models. ODE-based models integrate a pair of equations, one describing the acceleration of the object and the other the rate of mass loss (Opik, 1958; Silber et al., 2018). They are semi-analytic in nature, fast running, and useful for large ensemble studies of risk (Mathias et al., 2017). Several different ODE-based models have been developed with varying conceptualizations of the break-up process (Chyba et al., 1993; Hills and Goda, 1993; Ceplecha and Revelle, 2010; Popova et al., 2011; Avramenko et al., 2014; Wheeler et al., 2017; Register et al., 2017). All however require the user to specify a number of tuning parameters. In practice, the tuning parameters are typically fit to Chelyabinsk data, extrapolated from observations of meteors, derived from results of high-fidelity hydrocode simulations, or some combination of the three. Hydrocodes, on the other hand, begin with a material model and explicitly evolve the object's deformation due to its interaction with the atmosphere according to the inviscid Euler equations supplemented by models for strength, damage, porosity, et cetera. One of the biggest assumptions is that the material models accurately represent the bulk properties of the asteroid. Hydrocode simulations of asteroid airbursts are computationally expensive but can be quite valuable given the dearth of real-world asteroid airburst data. Likewise, these simulations can provide a window into the dynamics which drive the breakup process. Recently, high-fidelity hydrocode simulations have been used in efforts to reconstruct feasible size, composition, and entry characteristics consistent with the limited information we have regarding Tunguska's effects (Boslough and Crawford, 1997; Robertson and Mathias, 2019). If hydrocodes are to be used to make inferences about airburst events given minimal data, it is important to confirm these codes are appropriately modeling the relevant physics. This is likewise true if their results are to be used to inform parameter selection for fast running tools. In both cases, validation is essential to anchor the chain of analysis.

The Fluid Solid Interface Smoothed Particle Hydrodynamics (FSISPH) solver is one hydrocode used to model the atmospheric entry and breakup of asteroids and comets. The FSISPH package is part of Spheral++ and is based on a modified implementation of the smoothed particle hydrodynamics (SPH) method (Owen et al., 1998; Owen, 2010; Pearl et al., 2022). The formulation was developed to more accurately handle impacts between dissimilar materials with asteroid airbursts being the target application. The solver has been previously validated on a suite of shock, mixing, multi-material, elasticity, plasticity, and fracture problems (Pearl et al., 2022). The tests in the suite were selected to validate the solver on different aspects of the physics relevant to asteroid airbursts. For example, shock problems such as Sod,[1] Sedov,[2] and Noh[3] were selected as representatives of the hypersonic bow shock, diametral compression is a close analog for the stress state and failure model of an idealized spherical asteroid (Zaytsev et al., 2021; Rulko et al., 2025), and the breakup of a water column in a shock tube (Sembian et al., 2016; Xiang and Wang, 2017) served as a stand-in for the aerodynamic breakup of an asteroid in the limit of zero strength. FSISPH was later applied to model the Chelyabinsk event in a case study comparing the simulation-based energy deposition profile to those derived from observation (Brown et al., 2013; Popova et al., 2013; Pearl et al., 2023). Peak energy deposition agreed to within a few kilometers and leading fragment velocities showed good agreement with observation. The Chelyabinsk event, however, is not sufficiently well constrained to serve as a proper validation case. Though meteorites have been collected and their material properties characterized, they are biased by survival and thus not an accurate representation of the object's properties prior to entry. Moreover, the shape is unknown, and the best estimates of the diameter have a large uncertainty (Borovicka et al., 2013; Borovicka, 2015). For asteroid airburst codes, a piecemeal approach to validation is the only option as neither Tunguska nor Chelyabinsk are sufficiently well constrained to serve as rigorous validation exercises.

In this paper, we validate FSISPH's ability to model the dynamics of interacting solid objects in a supersonic flow by recreating the wind tunnel experiments of Laurence et al. (2012). Laurence et al. (2012) tracked the flight-path of two, initially-contacting, spheres in a Mach-4 flow, varying the relative sizes and orientation of the spheres. In the Chelyabinsk simulations of Pearl et al. (2023), the asteroid split into multiple interacting coherent fragments, consistent with observations of the event (Borovicka et al., 2013). The experiments of Laurence et al. (2012) serve as a well-posed analog for aspects of this phase of the airburst process- i.e. the separation and entrainment of fragments post-fracture (Register et al., 2020). This is not to suggest that two-sphere separation serves as an appropriate analog for the entire airburst process or involves all the relevant physics, however, it does test a code's ability to model the forces on coherent solid objects immersed in a supersonic flow. This was a crucial gap in our validation suite prior to this work. The experiments also test a code's ability to model the phenomena of separation, entrainment, and shock-surfing which are dependent upon the bow shock geometry (Laurence et al., 2012; Register et al., 2020) and can influence post-fragmentation airburst dynamics (Passey and Melosh, 1980; Laurence et al., 2007). We do note that the Mach number of the experiment is lower than what is characteristic of asteroids entering Earth's atmosphere (Mach>11), and in the hypersonic regime high-temperature effects influence the bow shock geometry. To probe the extensibility of our results to higher Mach numbers, we also perform a series of analytical validation tests in the hypersonic regime. We model a Mach-18 flow around a cylinder, testing FSISPH's ability to accurately capture the theoretical bow shock geometry and post-shock state given a gamma-law equation of state. We also fit a gamma-law specific heat ratio to match results obtained with the Livermore equation of state (LEOS), a tabulated equation of state which accounts for some high-temperature properties of air. This dual effort of validating the aerodynamic loads on a two-sphere system and the bow shock geometry at hypersonic speeds increases our confidence in FSISPH simulations of asteroid airbursts, with emphasis on the dynamical motion of

[1] The Sod shock tube test refers to the common hydrodynamics test problem focused on the one-dimensional evolution of a pressure and density discontinuity between two ideal gases (Sod, 1978).

[2] The Sedov explosion test refers to the application of a point-source energy deposit in a uniform, ideal gas at zero pressure and the development of a shock which can be described analytically (Sedov, 1959).

[3] The Noh implosion test is a strong shock problem similar to the Sedov explosion test with an analytical solution, wherein the shock results from a radial collapse of an initially uniform, ideal gas (Noh, 1987).

post-fragmentation coherent objects.

2. Methods

2.1. Hypersonic bow shock geometry

One of the primary characteristics of hypersonic entry problems is the formation of a bow shock displaced some distance away from the leading edge of the entering blunt body. As the freestream Mach number increases towards infinity, the bow shock's asymptotic angle decreases and is 'pushed' closer to the blunt body (Billig, 1967; Bedarov et al., 2011). Within the scope of the asteroid breakup problem, the geometry of the bow shock affects the way the body may fragment. Experiments and simulations have shown that the precise geometry of shock-shock interactions between neighboring bodies in a supersonic flow can qualitatively affect the flight-paths – i.e. entrainment versus dispersal (Laurence et al., 2012; Register et al., 2020; Cardona and Lago, 2023). As a result, it is crucial to correctly model the bow shock geometry to avoid systemic bias towards entrainment or dispersal.

2.1.1. Analytic bow shock standoff and sonic region

For a gamma-law gas, the bow shock standoff distance has a closed-form analytic solution. Sinclair and Cui (2017) developed an equation for the shock standoff distance for an infinite cylinder,

$$\delta = \frac{\beta_s^2}{\theta_s^2 \cos\beta_s}\sqrt{\frac{2+(\gamma-1)M_\infty^2}{2\gamma M_\infty^2-\gamma+1}} = f(\gamma, M_\infty),$$

in which, δ, is standoff distance non-dimensionalized by the cylinder radius, β_s is the sonic angle – i.e. the angle between the stagnation point and the sonic point – θ_s is the compliment of β_s, and M_∞ is the freestream Mach number. The angles, β_s and θ_s, are functions of the Mach number and specific heat ratio, and as such δ is likewise a function of the specific heat ratio and freestream Mach number alone. As the freestream Mach number increases, the shock standoff decreases, and the subsonic region is 'reduced'. The sonic angle, β_s, is a function of the coefficient of pressure at the stagnation point, $C_{p,max}$, and the coefficient of pressure at the sonic point, C_{ps},

$$\beta_s = \frac{\pi}{2} - \arcsin\sqrt{\frac{C_{ps}}{C_{p,max}}},$$

which is an algebraic reorganization of modified Newton theory (Sinclair and Cui, 2017; Anderson, 2006). The pressure coefficients are functions of the specific heat ratio and freestream Mach number (Sinclair and Cui, 2017),

$$C_{ps} = \frac{2}{\gamma M_\infty^2}\left[\left(\frac{(\gamma+1)M_\infty^2}{2\gamma M_\infty^2-\gamma+1}\right)^{\frac{\gamma}{\gamma-1}}\left(\frac{1-\gamma+2\gamma M_\infty^2}{\gamma+1}\right)-1\right],$$

$$C_{p,max} = \frac{2}{\gamma M_\infty^2}\left[\left(\frac{(\gamma+1)^2 M_\infty^2}{4\gamma M_\infty^2-2\gamma+2}\right)^{\frac{\gamma}{\gamma-1}}\left(\frac{1-\gamma+2\gamma M_\infty^2}{\gamma+1}\right)-1\right],$$

We use both the shock standoff distance and the size of the subsonic region to confirm that FSISPH is accurately modeling expected bow shock geometries in 2D-XZ (two-dimensional in cartesian XZ coordinates) given a gamma-law gas equation of state. We present overlays of the simulated sonic Mach contour (Mach = 1) and the analytical sonic boundaries to compare the size of the subsonic region. This presents a secondary utility for our validation exercise since we can perform a qualitative analysis of the accuracy of the simulated bow shock geometry, not just the standoff distance. A representative schematic is shown in Fig. 1.

2.1.2. Air equations of state

The gamma-law gas equation of state relates the pressure, P, of an ideal gas to the density, ρ, specific thermal energy, u, and the ratio of specific heats, γ,

$$P = (\gamma-1)\rho\, u.$$

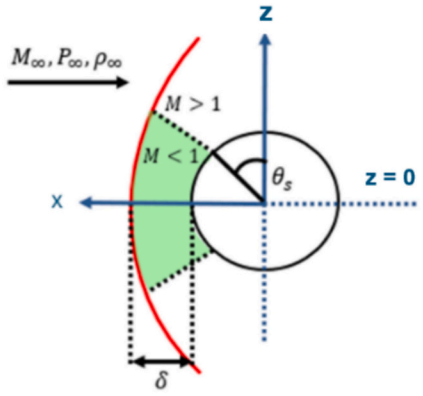

Fig. 1. Graphical representation of the quantities of interest in a bow shock development problem for spherical blunt bodies in high-speed flows. The red curve represents the bow shock, $\boldsymbol{\delta}$ is the bow shock standoff distance, and $\boldsymbol{\theta_s}$ is the inclination angle for the surface sonic point. The axis origin is centered on the body and z = 0 is the position oriented to the stagnation line. (For interpretation of the references to color in this figure legend, the reader is referred to the web version of this article.)

This equation is a form of the ideal gas law which implicitly assumes that the gas is calorically perfect – i.e. the specific heats, c_p and c_v, are constant. This is an acceptable assumption for subsonic and low-Mach-number supersonic flows, however, in the hypersonic regime, the air post-shock reaches very high temperatures causing the assumption to break down. At high temperatures, molecules in the air ionize, dissociate, and gain access to vibrational modes, in net, causing the effective specific heat ratio to decrease (Anderson, 2006). In this regime, the gas law with $\gamma = 1.4$ accurately reproduces the post-shock pressure but underpredicts the post-shock density and overpredicts the post-shock temperature (Anderson, 2006). In hydrocode simulations of atmospheric breakup, it is typically assumed that surface effects like ablation and heat transfer are negligible and that the dynamics are primarily driven by the pressure gradient (Lovering et al., 1960; Shepard et al., 1967; Raghunandan et al., 2022). This is justified through scaling arguments, the surface area to volume ratio decreases with increasing size and objects of interest from a planetary defense perspective are large (> 15 m diameter). As such, for a single coherent object, matching the surface pressure is most essential, and in this case, a gamma-law ratio with 1.4 is suitable. However, once there are multiple fragments interacting in a hypersonic flow field, it becomes important to match the shock geometry because it influences the motion of neighboring fragments.

A multispecies, reacting model of the flow is not available in Spheral and would be more computationally intensive. Alternatively, the tabulated Livermore Equation of State (LEOS) (Fritsch, 2016) accounts for these high-temperature effects, however, it is not available in the public version of Spheral and thus hinders reproduction of our results. To facilitate reproduction while still capturing appropriate high-temperature bow shock geometry, we tune the specific heat ratio in the gamma-gas law to match the shock standoff and density jump of LEOS at high Mach numbers. We will call this our "real-gas analogous specific heat". The fit is valid only at very high Mach numbers (Mach> > 5). This caveat is not an issue for our application as hydrocode simulations of breakup do not typically deal with velocities significantly lower than the entry velocity (Pearl et al., 2023). For both equations of state, we examine the effects of resolution. In our comparisons, we sample the density and pressure along the stagnation line running from the inlet to the stagnation point on the object. We then fit the data with

an arctangent function, like those used to estimate the step function behavior of sharp discontinuities indicative of a shock as shown in Kansa (1988).

2.1.3. Spheral model

We conduct our shock-geometry validation in 2D-XZ (two dimensional in cartesian XZ coordinates). We subject a 20-m-radius disk to Chelyabinsk-like conditions. The disk is treated as purely elastic with a density of 3.3 g/cc, shear modulus of 44 GPa, and bulk modulus of 105 GPa using the Tillotson equation of state (Tillotson, 1962). For this exercise, the object's material properties are not particularly important as it remains sufficiently stiff to appear rigid. The object is not allowed to damage or yield. The simulation starts at an altitude of 60 km and the freestream inflow conditions are set according to the US standard 1976 atm (NASA, 1976). The entry angle and velocity are 45 degrees and 20 km/s respectively. We run the simulation for 0.25 ms to get past the numerical startup phase and allow the bow shock to fully develop.

The computational domain consists of a rectangular region which is centered on the object. An upstream inflow condition feeds air nodes into the domain which are deleted once they cross the lateral or downstream domain bounds. The object is discretized with a circularly conformal distribution of equal-sized nodes. We set the resolution of inflowed air such that air nodes in the post-shock stagnation region have roughly the same volume as the object nodes. In our discussions of resolution, we parametrize the resolution in terms of the number of computational nodes spanning the radius of the object which we call the "nodes-per-radius". A detailed description of the model and implementation is presented in Pearl et al. (2023).

2.1.4. Calculating shock standoff and sonic region from simulation

We begin our analysis by interpolating the Mach number values from the SPH nodes onto a regular cartesian grid. We then use MATLAB to extract isocontours, using the Mach-10 isocontour as a proxy for the shock location. We then fit that contour with a fourth-order polynomial curve to estimate the global bow shock shape. This approach has been used in models of cosmological shock formations (Battarbee et al., 2020) and supersonic flow field experimental analysis (Jennis et al., 2025). To extract the standoff distance from the curve fit, we find its intersection with the stagnation line. See appendix for additional details on this analysis method and why Mach-10 was selected as a shock location proxy.

The freestream Mach number is parsed out by sampling the interpolated Mach grid at the inlet and taking a mean value. The Mach number and the specific heat ratio are then utilized in Sinclair's equations to determine the theoretical values for the sonic angle and bow shock standoff distance. The subsonic region is evaluated by finding the intersection point between the surface sonic point and the bow shock polynomial curve fit, assuming that the sonic line is perpendicular to the curve.

2.2. Laurence et al., 2012: supersonic spheres validation study

Laurence et al. (2012) examined the flight-paths of interacting spheres within a pressure-driven supersonic wind tunnel. Moreover, this experimental campaign focused on the correlation that interacting bow shock structures have on the dynamics of coherent objects in high-speed flow. In relation to our application of interest, these experiments are analogous to the interacting fragments often present in asteroid airbursts (Borovicka et al., 2013; Passey and Melosh, 1980). While a more 'realistic' scenario may involve more than two-body fragmentation events, multi-phase fragmentation, or the production of dust, the simpler model of two-sphere motion is an appropriate avenue for our validation efforts. Despite being representative of an 'idealized' scenario, the experiments are well-defined and concentrate specifically on the aerodynamic loads exhibited on bodies constrained by size and orientation. Therefore, these experiments serve as excellent validation cases to demonstrate that FSISPH can realistically model the flight-path of coherent body fragments. Future validation efforts can attempt to incorporate additional complexities associated with a broader scope of the airburst process.

Laurence and his team utilized the GALCIT Ludwieg tube (Mouton and Hornung, 2008), a pressure-driven free-jet facility, to generate a Mach-4 flow at a nominal pressure and density of 1.4 kPa and 0.07 kg/m3. In the test section of this experimental facility, they hung two nylon spheres (ρ =1120 kg/m3) of varying size ratios, relative to each other, via floss threads attached to the roof of the section. This permitted the spheres to remain suspended until the initial pressure-driven shock passes through the mounting threads and tears them off, allowing the binary system of spheres to develop interacting bow shocks and flow downstream. The larger sphere is referred to as the primary sphere and the smaller, the secondary sphere. The diameter of the primary was held constant at 25.4 mm throughout the experimental campaign. In some cases, the secondary sphere is initialized oriented at some degree away from the vertical. A schematic of this setup is shown in Fig. 2 and details on the cases we model are listed in Table 1.

2.2.1. Spheral model

We model all five radial ratio cases and all three secondary sphere orientation cases presented in Laurence et al. (2012), resulting in eight total configurations. A representative image of a simulation of one such case is presented in Fig. 4. In addition to modeling these eight cases with the FSISPH solver, we also model a singular case with Spheral's standard SPH package. A description of that SPH formulation can be found in Appendix E: Compatible Smoothed Particle Hydrodynamics, of Frontiere et al. (2017). As mentioned previously, FSISPH is built to specifically handle the interaction of dissimilar materials and the sharp density discontinuities that arise between dissimilar materials in high-speed flow settings. Modeling one of these cases without utilizing the FSISPH solver should make the distinction between the solvers readily apparent through simple qualitative analysis of the results. More details about the differences between FSISPH and Spheral's baseline SPH can be found in Pearl et al. (2022). Key parameters for the full set of simulations are detailed in Table 1.

Our simulations encompass a 3D hexahedral domain with dimensions 11 × 14 × 14 cm with the centroid located at (−2.5, 0, 1) cm relative to the center of the primary sphere. A reflection boundary condition is used for the lateral walls. The upstream boundary is modeled as an inlet that feeds particles into the domain at the freestream conditions with pressure $P = 1.4$ kPa, density $\rho = 0.07$ kg/m3, velocity v = 670 m/s, consistent with a Mach number of 4.0 (see Table 2). The

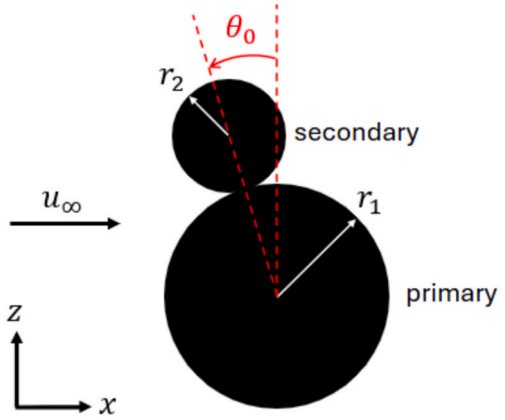

Fig. 2. Illustration of the experimental setup from Laurence et al. (2012). The secondary sphere is situated on top of the primary sphere. The dependent parameters of the flow experiments are the spherical radii ratio ($\boldsymbol{r_2/r_1}$) and the orientation of the secondary sphere with respect to the primary sphere, $\boldsymbol{\theta_0}$, along their center line axis, with $\boldsymbol{\theta_0 > 0}$ being towards the freestream flow.

Table 1
Configurations and discretization used in our simulations of the Laurence et al. (2012) experiments. In some simulations, the secondary sphere is initialized with a lateral velocity to model the impulse caused by the floss prior to detachment.

Radius ratio (r_2/r_1)	Angle (θ_0)	lateral velocity (m/s)	Resolution (mm)	Primary (nodes/radius)	Secondary (nodes/radius)	Solver	Laurence Case
1.0	− 0.6°	0.013	0.5	51	51	FSISPH	9e
0.75	− 1.1°	0.03	0.5	51	38	FSISPH	9d
0.625	− 0.7°	0.051	0.5	51	32	FSISPH	9c
0.625	− 1.9°	0.051	0.5	51	32	FSISPH	10a
0.625	4.1°	0.051	0.5	51	32	FSISPH	10b
0.625	22.8°	0.051	0.5	51	32	FSISPH	10c
0.5	− 0.1°	0.1	0.5	51	25	FSISPH	9b
0.25	0.4°	0.08	0.25	102	25	FSISPH	9a
0.25	0.4°	0.08	0.5	51	13	FSISPH	9a
0.25	0.4°	0.08	1.0	25	6	FSISPH	9a
0.625	− 0.7°	0.051	0.5	51	32	SPH	9c

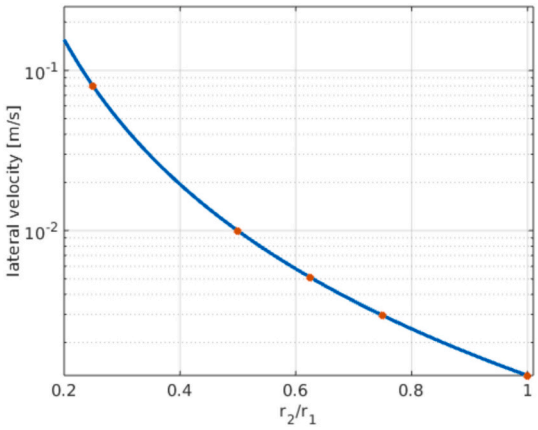

Fig. 3. The associated lateral velocity impulse imparted upon the secondary sphere assuming a 0.12e-4 [Newton-second] single thread impulse imparted instantaneously only in the vertical direction.

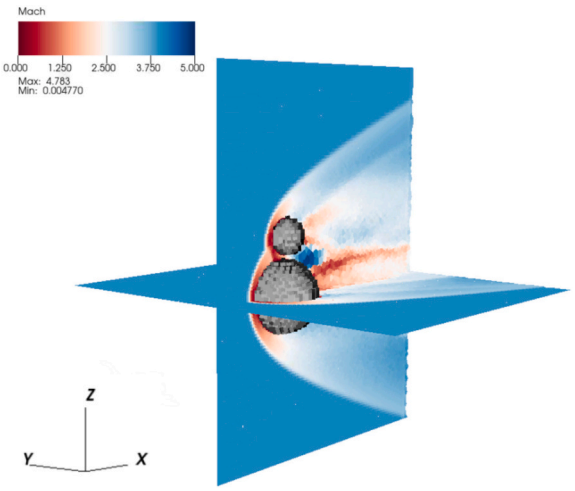

Fig. 4. An isosymmetric slice in the x-z plane of the 3-dimensional two sphere interaction in supersonic flow problem as modeled in Spheral. This frame is from the simulation modeling case 9b in Laurence et al. (2012).

Table 2
Freestream air gas inflow conditions based upon the typical test conditions as reported in Laurence et al. (2012).

Pressure [kPa]	Density [kg/m3]	Sound Speed [m/s]	Velocity [m/s]	Mach
1.4	0.07	167	670	4.0

implementation of the inflow condition is described in Pearl et al. (2023). Particles are deleted once they pass the plane defining the downstream extent of the domain. On simulation start up, air nodes are initialized at the freestream inflow condition and the spheres are initialized at zero pressure. Nominally, both spheres are initialized as stationary, however, we optionally model the impulse from the floss prior to separation by initializing the spheres with a non-zero velocity. The impulse velocity is a function of the spherical body size and the values are listed in Table 1. The lateral impulse imparted by one torn floss thread was found to be 0.12e-4 Newton-second, which corresponds to a lateral velocity impulse upon the spherical bodies, as shown in Fig. 3. The figure demonstrates that the floss thread detachment has the largest effect on the lateral velocity of the smallest of the secondary spheres. The axial impulse was found to be negligible due to the geometrical nature of the floss detachment.

The FSISPH solver treats different materials via a fully-coupled SPH framework and thus the different behaviors of different materials are derived from their different equations of state and strength models. We model air as an ideal gas using the gamma-law gas with a specific heat ratio of 1.4. We model the spheres as perfectly elastic bodies using the Murnaghan equation of state with exponent $n = 1$, bulk modulus K = 100 MPa, and density ρ=1120 kg/m3 and a constant strength model with Poisson ratio of 0.2 and an effectively infinite yield strength. This bulk modulus was not selected to correspond with the physical bulk modulus of nylon, but rather, it was selected to be high enough to ensure quasi-rigid behavior without adversely affecting the simulation's time step. In this experiment, elastic deformation of the spheres is not expected to meaningfully alter the dynamics and thus the moduli only need to be stiff enough to enforce quasi-rigid behavior.

To discretize the air, we use a cartesian lattice of nodes with holes punched out to accommodate the two spheres. The holes' radii are 5% larger than the spheres. To discretize the spheres, we use the recursive primitive refinement scheme of Raskin and Owen (2016) as implemented in Spheral's RPRPS generator. This creates a spherical-conformal distribution of roughly equal-sized nodes. The resolution of the sphere nodes parameterizes the resolution of our simulation. The initial air-lattice resolution is set up to be coarser than the spheres by a multiplicative factor of $(\gamma + 1)/(\gamma - 1)$. This accounts for the compression of the air nodes by the bow shock resulting in air and sphere nodes that are roughly volume-matched near the stagnation point. To prevent singular configurations, we randomly perturbed the air nodes from their lattice positions with a maximum magnitude of 0.5% the lattice spacing.

2.2.2. *Validation metrics*

To assess how well our simulation matches the experiment, we compare the relative velocities of the two spheres as a function of time. In our simulations, we output the center-of-mass positions and velocities of both spheres at 100 μs intervals and model a total of 10 ms. To determine the experimental velocities, we implement a visual tracking algorithm in MATLAB and apply it to process the raw image frames from

the 2012 experimental campaigns. This method is similar to the one developed by Laurence and Karl (2010) to track the motion of a free-flying body over a sequence of high-speed video captures.

In our implementation of the tracking algorithm, we import the experimental video frames into MATLAB, and utilize the image processing toolbox, specifically the circle detection method by Atherton and Kerbyson (1999), to detect the spherical edge points to a pixel resolution. By detecting the two circular shapes every frame, we then back out an average pixel length diameter for each sphere and plot the relative pixel-per-second motion of both spheres in the axial and lateral directions. To evaluate the uncertainty in our measurement methods, we utilize the Kline and McClintock (1953) error uncertainty method for single sample experiments. This method remains valid as long as the uncertainty in measured values are independent of each other. Since our uncertainty value is for the relative velocity of the spheres, the two errors that propagate in those evaluations are the pixel-based circle tracking uncertainties and the spherical measurement uncertainties presented by Laurence et al. (2012).

3. Results

3.1. Hypersonic bow shock – 2D circular model

Table 3 contains the standoff distances evaluated from eq. 32 ($\delta_{sinclair}$) (Sinclair and Cui, 2017) and those estimated from the bow shock fitting scheme (δ_{FSISPH}) using both the LEOS tables and the manually set gamma-law gas value. As we increase the nodes-per-radius resolution parameter, the computational thickness of the shock does decrease, however, in lieu of a definitive boundary between the freestream and post-shock region, we estimate the placement and geometry of the bow shock by applying a curve fit model to the data. A resolution study for the LEOS table simulations demonstrates that the standoff distance converges towards a delta of approximately 0.25, or a distance that is one-eighth of the body diameter. Comparatively, the standoff values for the case where the specific heat ratio is set to the ideal condition of 1.4 are markedly different from what is demonstrated by the LEOS modeled simulations. This underlines an important fact that will be explored further in this subsection: the physical problem that we are modeling exists in a regime where high temperatures generated from high-speed flow environments around blunt bodies render the ideal gas law inaccurate.

A closer look at the cases where the ratio was set to 1.25 and 1.2 for the 30 nodes-per-radius parametrization demonstrates that those standoff values bracket the one determined for the LEOS modeled case. A higher resolution study for the 1.2 ratio case demonstrates that the delta value convergences to within 6% of the delta determined for a similar LEOS case and within 13% of the delta for the highest resolution LEOS case. This difference jumps to within 9% and 30%, respectively, for the 1.25 ratio case. What this seems to indicate at first inspection is that the appropriately matching specific heat ratio for this problem scenario is likely somewhere between 1.2 and 1.25. We do not list the Sinclair evaluated standoff for the LEOS cases because the specific heat ratio is variable in this tabulate EOS and the equation from Sinclair and Cui assumes a constant specific heat ratio.

Fig. 5 displays the contours of Mach = 1 and 10, the bow shock polynomial curve fit, the theoretical subsonic region, as highlighted in green, and the theoretical shock standoff distance, displayed by a vertical red line, for two resolution cases of the gamma-law gas EOS, $\gamma = 1.2$. Qualitatively, we can immediately discern that, for both resolution cases presented here, the theoretical subsonic region adequately contains the crescent shaped sonic contour of the post-shock region near the leading edge of the body. This observation extends to the results from the $\gamma = 1.25$ and 1.4 simulations, as presented in the Appendix. Upon observation, these qualities, alongside what we've learned of the standoff evaluations, demonstrate appropriate bow shock modeling achieved by the solver.

We perform additional analysis on these simulations in order to determine a real-gas analogous specific heat ratio; we sample data along the stagnation line and compare physical air properties between the gamma-law gas modeled cases and the LEOS modeled cases. A summary result of these efforts is shown in Fig. 6. More comprehensive results are presented in the Appendix.

To reiterate, in a high-speed flow environment, ionization and dissociation effects cause divergence from the ideal gas theorem since gas can no longer be considered diatomic. Utilizing the ideal gamma-law gas value of 1.4 causes an overprediction of temperatures and an underprediction of densities behind Mach >5 shocks. Since the LEOS tabulations account for these high temperature effects, we use those results as our baseline in order to determine an appropriate representative specific heat ratio that can be used to model comparative post-shock densities without necessarily modeling high-temperature air chemistry. The standoff distances evaluated using the specific heat ratio in lieu of the LEOS tabulations estimate that the representative ratio is somewhere between 1.2 and 1.25. Analyzing the stagnation line curves demonstrates that this was a decent assumption. The 1.25 ratio underestimates the density of air at a higher magnitude than the 1.2 ratio. If we simply overlay the LEOS, 60 nodes-per-radius resolution case with the 1.2 gamma-law gas ratio, 60 nodes-per-radius resolution case, we would observe an exceptional overlap.

Finally, we can discern the outlying shock discontinuity behavior for the ideal gas law simulations utilizing $\gamma = 1.4$ and discuss the appropriateness of modeling these problems with the ideal gas assumption. The density values are grossly underestimated, and the standoff distance is overestimated. Both conditions can have significant effects on how fragments move in the hypersonic flow. The asteroid body does not simply break apart, its constituent objects form their own bow shocks and interact with each other, affecting their relative motion. As will be discussed in greater detail in the next section, the shock geometries of independent fragments interact with each other, leading to dynamical behaviors readily dependent on shock structure and, therefore, the physical properties of air in the post-shock region.

3.2. Flow-structure interactions – 3D spherical model

Fig. 7 displays the primary and secondary body positions modeled with Spheral and overlaid onto their respective experimental frames from the Laurence et al. (2012) studies. The overlay is initialized by centering the starting positions of the bodies in Spheral onto the centers of the two bodies in the video at around the time that the floss threads initially break and the bow shocks begin to form, indicating that the tunnel has started up supersonic flow. The cases presented for overlay are 9a, 9c, and 9d. These cases were chosen because they represent the

Table 3
Standoff distance values in meters for nine distinct Spheral simulations, varying resolution and/or EOS. The absolute difference between the computed standoff distance (δ_{FSISPH}) and the standoff distance as evaluated by eq. 32 ($\delta_{sinclair}$) in Sinclair and Cui (2017) is presented in the bottom row for the gamma-law gas cases.

	LEOS			$\gamma = 1.4$		$\gamma = 1.25$		$\gamma = 1.2$	
resolution	30	60	120	30	60	30	60	30	60
$\delta_{sinclair}$	–	–	–	9.01	9.01	6.42	6.42	5.53	5.53
δ_{FSISPH}	7.62	5.92	4.96	10.15	8.80	7.75	6.41	6.92	5.60
$\lvert\delta_{sinclair} - \delta_{FSISPH}\rvert$	–	–	–	1.14	0.21	1.33	0.01	1.39	0.07

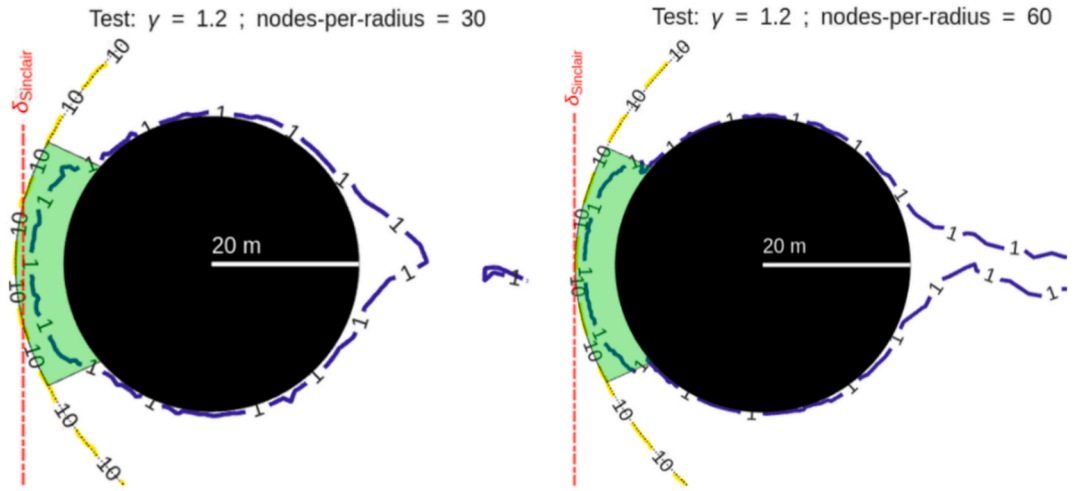

Fig. 5. Visualizations of the contour fields for Mach = 1 and 10 and the fourth-order polynomial curve fit to the Mach-10 contour. The left panel shows results for a lower resolution case of 30 nodes-per-radius and the right panel shows a higher resolution case at 60 nodes-per-radius. The green overlay represents the theoretical subsonic zone as determined by evaluation of the sonic angle. The red vertical line represents the theoretical shock standoff distance as determined by the closed form analytic solution from Sinclair and Cui, 2017. (For interpretation of the references to color in this figure legend, the reader is referred to the web version of this article.)

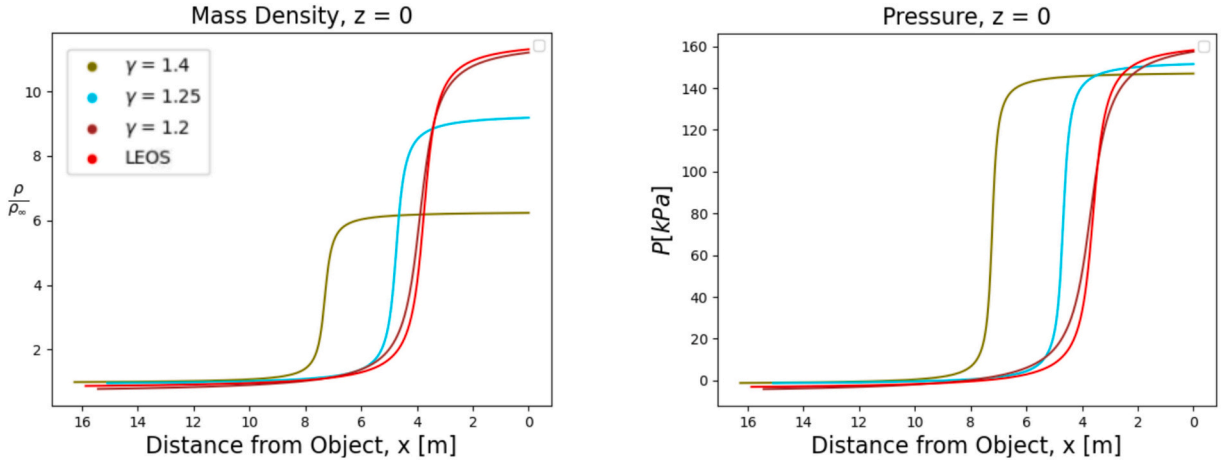

Fig. 6. (Left) Mass density values across the shock, along the stagnation line, normalized by the freestream density for LEOS modeled case and specific heat ratios of 1.2, 1.25, and 1.4 at 60 nodes spanning the circular radius. (Right) Pressure across the shock, along the stagnation line. Note, flow direction is from left to right in these figures and z = 0 indicates the object's stagnation line.

three characteristic behaviors of fragment-body motion in supersonic flow: entrainment, shock-surfing, and expulsion, respectively. Qualitatively, the overlay of the simulation results with the experimental footage implies that the hydrocode solver we have been using does an adequate job properly capturing these behaviors.

Fig. 8 plots the lateral and axial motion of the primary and secondary spheres relative to their starting position for cases 9a and 9c. Similar plots for the other three cases can be found in the appendix. Across all of the baseline simulations, as introduced in the methods section, the spheres are discretized at a resolution of 500 μ m. This equates to 51, 38, 32, 25, and 13 nodes-per-radius for diameters of 25.4, 19.05, 15.88, 12.7, and 6.35 mm, respectively. Our resolution study in the 2-dimensional cylindrical body cases suggested that 30 nodes-per-radius is under-resolved. This issue is immediately apparent in the simulation results representative of case 9a for the secondary body in both the lateral velocity (V_z) and axial velocity (V_x) curves. Comparatively, both the primary spherical body lateral and axial velocity curves most closely resemble the relative velocity plots generated from the experimental video frames, indicating that 51 nodes-per-radius is sufficiently resolved to capture the flight-paths of the spheres.

Likewise, the secondary sphere axial velocities, for cases 9b through 9e, demonstrate remarkably similar behavior to the experimental axial velocities. As described by Laurence and Deiterding (2011) it is the lateral velocity term that dominates the shock-surfing behavior of multi-body interactions in a high-speed flow. For the cases where the radii ratio is greater than 0.25, the lateral velocity curves for the secondary sphere demonstrate reasonable agreement with the respective experimental lateral velocity curves. The largest lateral velocity discrepancies exist for cases 9a and 9b, corresponding to secondary body ratios of 0.25 and 0.5 relative to the primary body. These spheres, modeled with nodes sized 500 μ m, are discretized with 13 and 25 nodes-per-radius respectively. This implies that the main reason for these lateral velocity discrepancies may lie in the resolution of the smaller body. Additionally, the lateral impulse force imparted on the secondary body tends to be much higher for the smaller ratio cases and any uncertainty in that impulse would propagate to the initialized velocity in our simulations.

We conduct a resolution study on case 9a to investigate these discrepancies. Two additional simulations were conducted for the radii

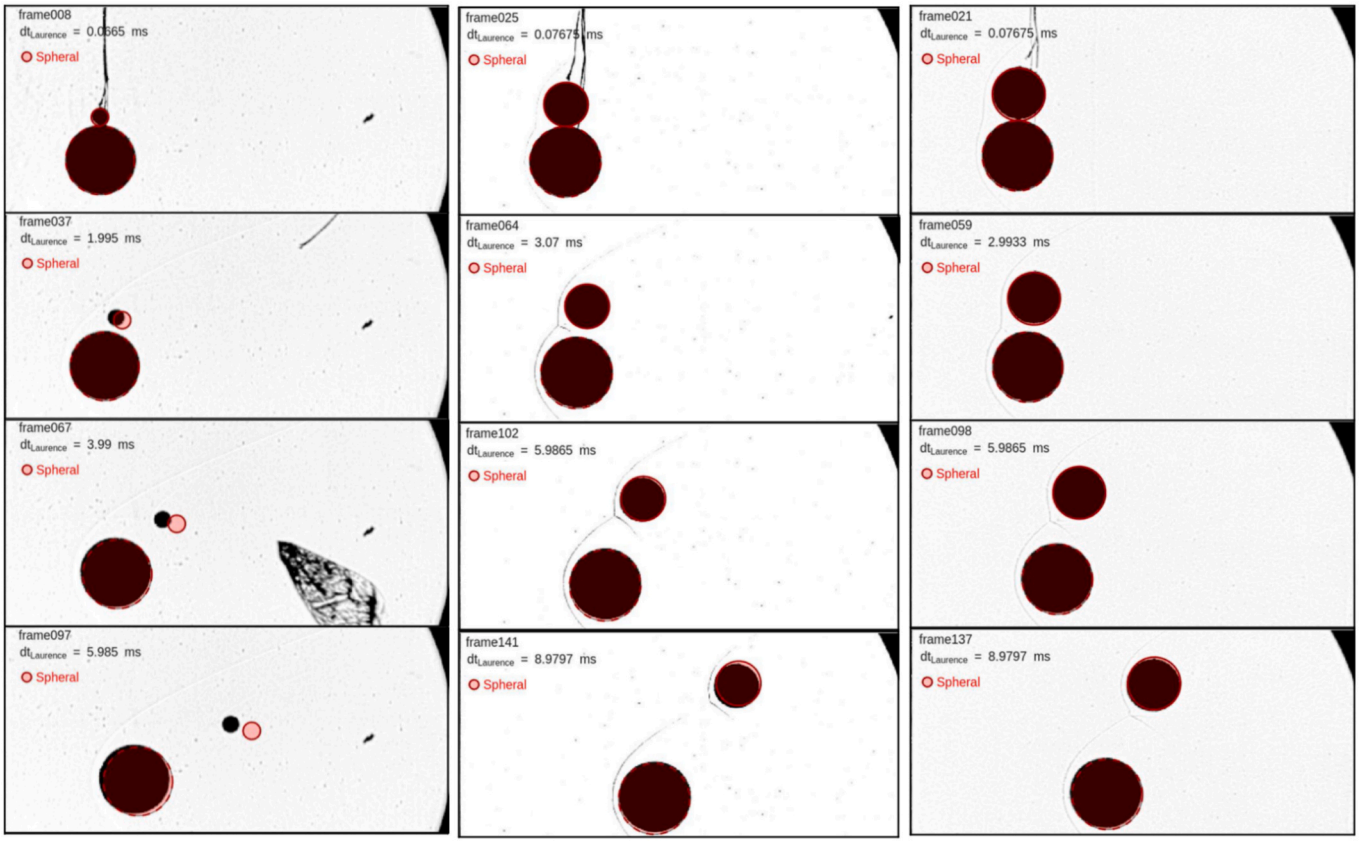

Fig. 7. Overlay of the experimental footage and Spheral results for: (Left) Case 9a (Middle) Case 9c (Right) Case 9d at 0.500 mm nodal resolution. The time evolution of each case is shown going from top to bottom in each column.

ratio case 9a (0.25), which had both the largest lateral and axial velocity discrepancy. A coarser resolution of 1 mm was selected to generate a velocity curve diagram that could be used to demonstrate the convergence of the value of interest. This coarse model is reflective of 6 node-per-radius discretization of the secondary spherical body. A finer resolution of 250 μ m, in which the secondary body's resolution is 25 nodes-per-radius was selected as well. The results of this resolution analysis are presented in Fig. 9. The lateral velocity curve demonstrates convergence that does not quite match the error margin of the curve derived from the experimental case footage. Despite this, we can acknowledge that the solver does an adequate job of properly simulating the entrainment behavior for this ratio case. It seems that the secondary body motion would be more sensitive to small perturbations since the shock-surfing behavior may act as a mathematical saddle point in the dynamical landscape. Perturbation can induce a transition from this saddle point into a region where the body would experience entrainment or expulsion and the model resolution can act as a form of perturbation, as shown by the earlier induced entrainment in the coarser simulation. However, the primary body doesn't have the same saddle point in its dynamical landscape and would be less sensitive to small perturbations, evidenced by the accuracy we retain in both the lateral and axial motion for all three resolution cases.

We also modeled the three cases where the secondary sphere has varying initial alignment with respect to the primary sphere. The secondary spherical radii are held constant at a ratio of 0.5 to the primary sphere and defined by 500 μ m nodes. Similar to the varying radii cases shown in Fig. 8, the varying orientation cases shown in Fig. 10 demonstrate that the computed axial velocity curves match well to the curves from the experimental footage. The primary focus is on the lateral velocity curves and any noticeable discrepancy. The computed lateral velocity curves exhibit better agreement with the experimental curves as the secondary body is oriented closer to the freestream flow, towards the leading edge of the primary body. Once again this implies a greater sensitivity of the dynamical motion of the secondary body in relation to the shock-surfing behavior.

Secondary spherical orientation mainly affects the secondary sphere dynamics by way of changing the lift-to-drag ratio in a manner similar to what is experienced by the sphere when changing the relative size ratio between the two spherical bodies. In both continuum and rarefied flow regimes, bow shock-surfing behavior causes these differences in the aerodynamic forces on the secondary sphere (Laurence and Deiterding, 2011; Cardona and Lago, 2023). As the secondary sphere is entrained in the wake of the primary body, the dynamics become drag dominated. Likewise, the drag coefficient dominates the aerodynamic motion when the secondary sphere is expelled into the freestream flow. However, there is a point at which the lift coefficient has a significant impact on the dynamics of the lateral motion of the secondary body and that is when the secondary sphere 'surfs' the primary body shock. When the secondary body is oriented further into the freestream, it develops its own bow shock and the interaction between its shock and the primary body shock is limited temporally and spatially, so little lateral force is applied to the sphere. However, there exists a transition, where the secondary body maintains this shock-to-shock interaction much further downstream. Orientation or radii ratios below this transition demonstrate that the secondary body surfs the primary body shock but is pushed into the wake. A consequence of this is that the secondary sphere exhibits some lateral velocity at the start but has an imparted lateral force in the opposite direction, creating a downward acceleration. It seems to be this deceleration, related to the shock-shock interaction, that drives the discrepancy for cases 9a, 9b, and 10a.

Finally, we performed an additional simulation of case 9c but with the standard SPH solver available in Spheral instead of FSISPH (see

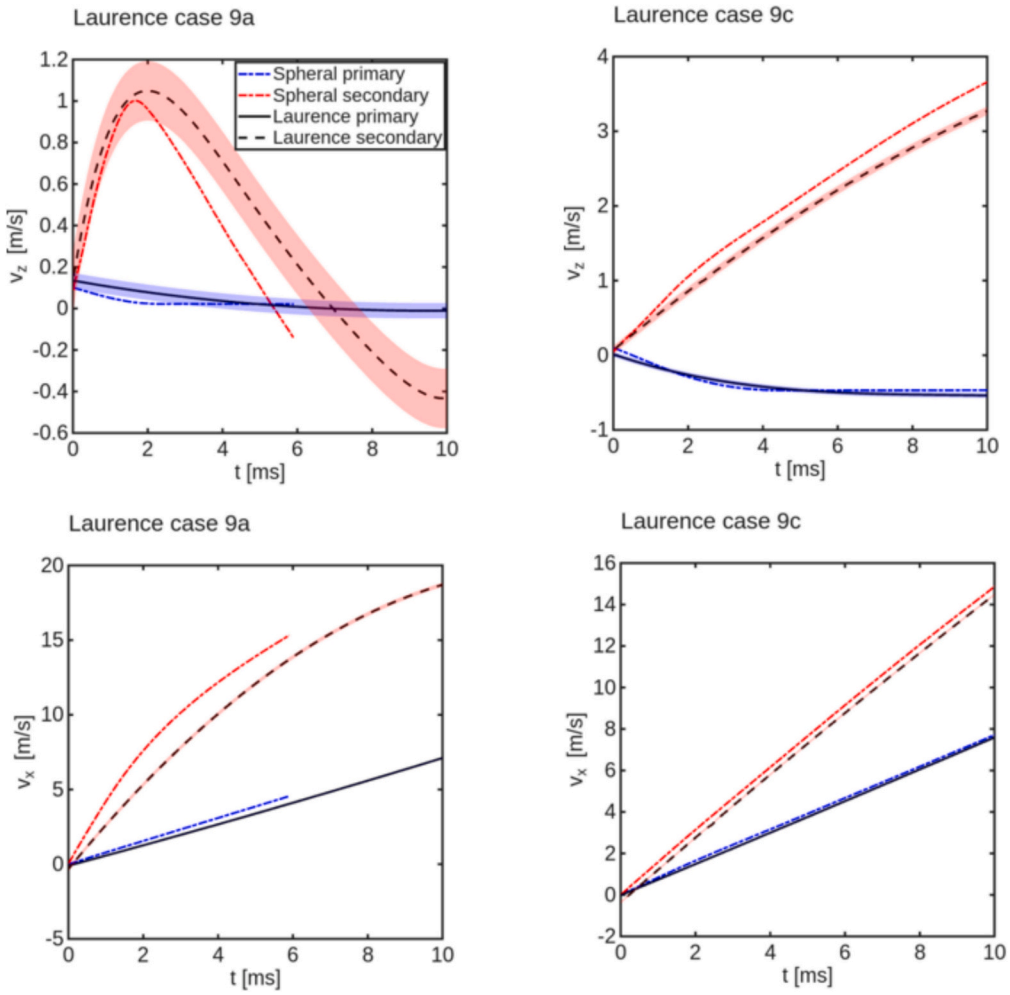

Fig. 8. (Left) Results representative of case 9a ($\frac{r_2}{r_1} = 0.25$) in Laurence et al. (2012). (Right) Results representative of case 9c (0.625).The top row represents the lateral velocity of the two spheres relative to their starting positions, the bottom row represents the axial velocity in a similar fashion. The red shaded region represents our uncertainty quantifying the motion of the nylon spheres from the experimental footage.

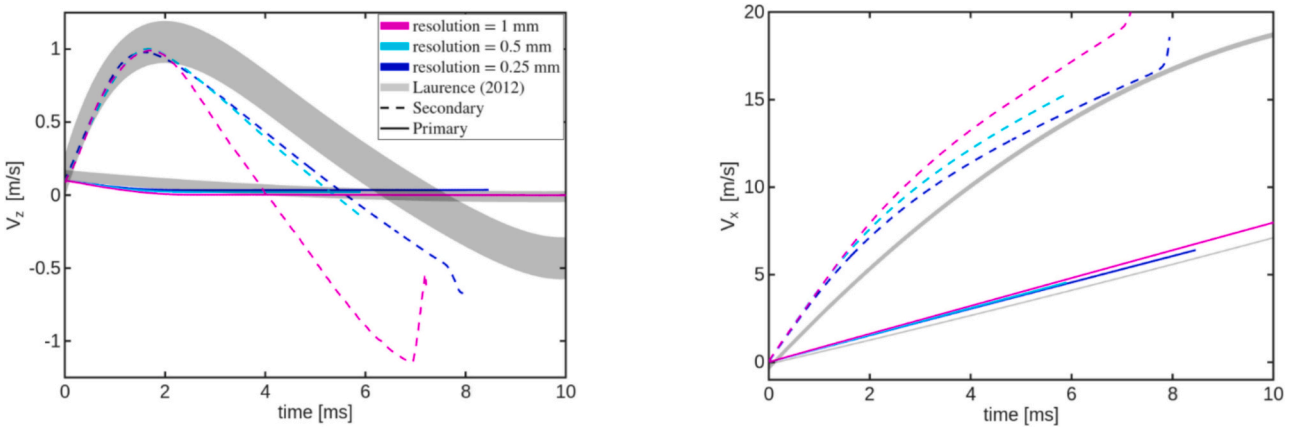

Fig. 9. Resolution case study for Laurence et al. (2012) case 9a ($\frac{r_2}{r_1} = 0.25$) incorporating a lateral impulse. The diameter of the secondary sphere is approximately 6.4 mm. The global resolution for the standard simulations presented here are 1 mm, 500 μm, and 250 μm indicating that the sphere has approximately 6, 13, and 25 nodes-per-radius, respectively. The shaded region represents the motion of the spheres as determined from the experimental footage, including the measurement uncertainty.

Fig. 11). The intention was to demonstrate the abilities of the FSISPH solver by comparing its performance to a solver that is not dedicated towards modeling dissimilar materials with large property discontinuities in a high-speed flow. What we demonstrate here is that the standard SPH solver fails to acceptably model either the lateral or axial velocities of the two spheres. Additionally, the Spheral results

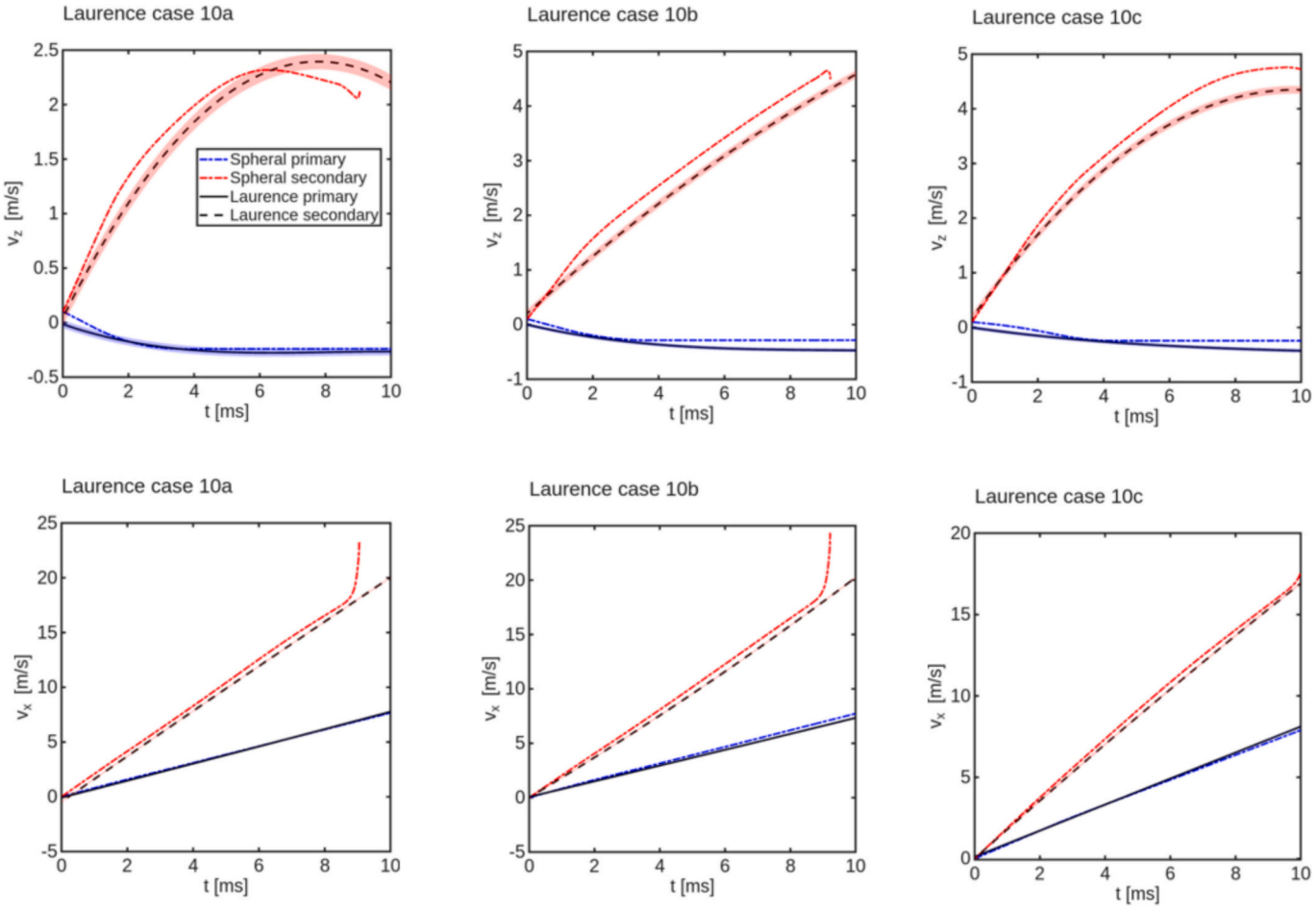

Fig. 10. The lateral and axial velocities of the two spheres relative to their starting position orientation. From left to right, representing cases 10a (θ_0 = -1.9), 10b (4.1), and 10c (22.8).

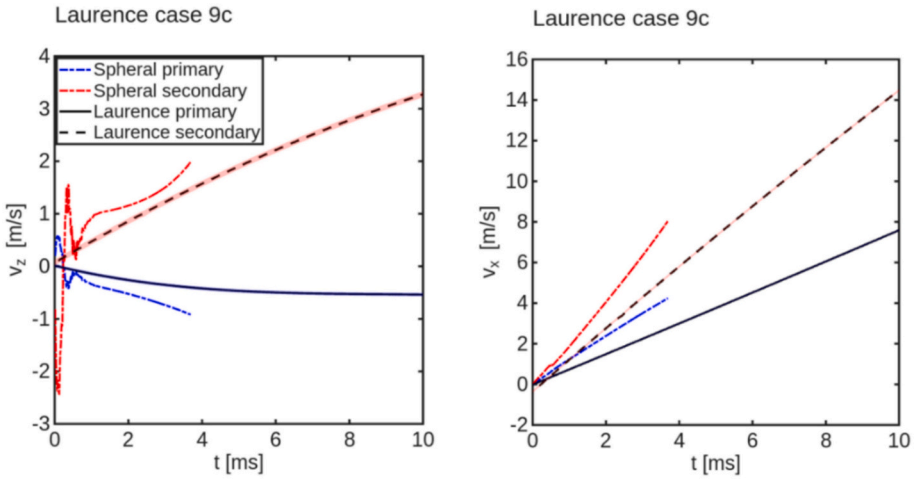

Fig. 11. (Left) Lateral and (Right) axial relative velocity curves for the two spherical bodies utilizing the baseline SPH solver. Solver encountered a time-step error at around the 4 ms mark.

curve is cut short at around 4-ms which is indicative of a time-step error encountered during the simulation and a consequence of the inability of the solver to handle such flow environments.

4. Conclusions

In this paper, we focused on extending the validations of Spheral's FSISPH solver for the application of asteroid airburst events. We examined the ability of FSISPH to accurately model the flight-paths of interacting solid objects in a supersonic flow by recreating the wind

tunnel experiments of Laurence et al. (2012). We also examined the solver's ability to model the geometry of a hypersonic bow shock by making comparison to analytic expectations in the limit of very high Mach numbers. The experiment of Laurence et al. serves as an analog for the interacting fragments of asteroids during an airburst event. The experiments also highlight the importance of the bow shock geometry in determining whether fragments are entrained behind the main body and how aerodynamic forces influence fragment motion. As such, these are crucial physics that a hydrocode targeting this application should accurately represent.

In our validation of the shock structure, we found FSISPH reproduces the expected shock stand-off from analytic theory given a gamma-law gas equation of state. Qualitatively, the overlay of the theoretical subsonic post-shock region with the sonic contours from the simulation demonstrated excellent agreement, further reinforcing the validity of the simulated shock geometry. For the high-Mach-number regime of atmospheric entry, we found that a specific heat ratio of 1.2 is more appropriate than the nominal 1.4 typically used for supersonic applications. A specific heat ratio of 1.2 recreates important net effects of the non-ideal behavior of air at high temperatures – i.e. a smaller shock standoff and higher post-shock density. The gamma-law gas equation of state with a specific heat ratio of 1.2 compared well with the tabulated Livermore Equation of State and has the added benefit of simplifying the reproduction of our results. It should be noted however that care must be taken to adjust the specific thermal energy to ensure the appropriate inflow pressure.

In our validation of the multi-body interacting motion, we found that FSISPH was able to recreate the experimental results of Laurence et al. and demonstrate the solver's ability to accurately model interacting rigid bodies in a supersonic flow. A qualitative analysis found that the secondary sphere's motion is sensitive to small perturbations, especially if the body is either smaller than the primary or oriented in a manner that induces shock-surfing behavior. The aerodynamical loads on the secondary body while it travels along the primary body shock seem to dominate the expulsion or entrainment process, for which the shock-surfing regime serves as a boundary. FSISPH's ability to accurately capture the shock-surfing boundary observed in experiments suggests airburst simulations run with FSISPH are not biased towards either expulsion or entrainment. In addition, the results generated for case 9c modeled with a standard SPH solver further highlight the unique efficacy of the FSISPH solver in accurately capturing multi-body motion in high-speed flow.

The utility of these validation tests was to independently demonstrate the application of the FSISPH solver towards problems comprising key attributes of the dynamical nature of asteroid airbursts. In order to model case studies such as Chelyabinsk or Tunguska, it is necessary to verify as many individual physical processes associated with the airburst as possible, since no real-world airburst is sufficiently well constrained to serve as a true, integrated, validation case. In lieu of such comprehensive benchmark data from an airburst event, we concentrated on two practical exercises to demonstrate the capability of the solver in modeling asteroid entry and fragment dynamics. The analytical bow shock exercise and the two-sphere motion exercises showcase the solver's ability in accurately modeling both the hypersonic entry conditions and the entrainment/expulsion aerodynamic mechanism. Together, this work increases our confidence in the FSISPH's ability to model the flight-paths of coherent fragments in asteroid airburst simulations.

CRediT authorship contribution statement

Veronika A. Korneyeva: Writing – review & editing, Writing – original draft, Visualization, Validation, Investigation, Formal analysis, Conceptualization. **Jason M. Pearl:** Writing – original draft, Supervision, Software, Methodology, Conceptualization. **Kathryn M. Kumamoto:** Writing – review & editing, Project administration. **J. Michael Owen:** Writing – review & editing. **Cody D. Raskin:** Writing – review & editing. **Megan B. Syal:** Writing – review & editing, Project administration. **Nicholaus J. Parziale:** Resources. **Stuart J. Laurence:** Resources.

Declaration of competing interest

None.

Acknowledgments

This work was performed under the auspices of the U.S. Department of Energy by Lawrence Livermore National Laboratory under Contract DE-AC52-07NA27344, LLNL-JRNL-2008750.

We would like to thank Professor Stuart Laurence and Professor Nicholaus Parziale for providing the experimental footage documented in their 2012 publication “Dynamical separation of spherical bodies in supersonic flow.” Their collaboration has been an invaluable utility towards Lawrence Livermore National Laboratory's planetary defense research goals.

Appendix A. Appendix

A.1. Validity of the continuum

During entry into the atmosphere, as the asteroid body moves through the transitional zone (approximately 90 km to 140 km), it typically transitions from a free molecular flow state to a continuum (Campbell-Brown and Koschny, 2004). In a continuum flow regime, where the Knudsen number is less than 0.01, a shock forms in front of the asteroid body. For the size class of airburst capable asteroids that we are interested in, we can conventionally consider a 90 km altitude as the upper limit to ensure continuum flow, above which the mean free path begins to increase by several orders of magnitude (Moss and Bird, 1984; Gamgami et al., 2009). This is supported by previous studies into the ablation of faint meteors where bodies of 1 m diameter are considered in continuum flow below 110 km assuming an increase in body density over atmosphere (Campbell-Brown and Koschny, 2004). For example, utilizing the characteristic length of 20 m at 100 km altitude, for which the free mean path is approximately 0.1 m (NASA, 1976), the Knudsen number evaluates to 0.005 which is within the continuum region. In general, we don't model above 100 km altitude and the dynamics of the airburst process don't necessarily become prominent until the body is within 40 km of the ground.

One additional validation that we can include, knowing the viable real-gas specific heat ratio, is confirmation that we are performing our validation techniques within a continuum flow regime. The nature of the flow, either rarefied or continuum, can have marked effects on the body drag coefficient and bow shock geometry thereby affecting the aerodynamic interactions of fragmented bodies. We can perform two Knudsen number evaluations based upon the parameters determined from the simulations described in section 3.1 to ensure that our assumption of operating within a continuum flow regime is accurate,

$$Kn = \frac{\lambda}{L} \text{ and } Kn = \frac{M}{Re}\sqrt{\frac{\pi\gamma}{2}}$$

To re-emphasize the importance of this validation, the Euler equations of fluid motion are only valid in the continuum flow regime, approximated by a Knudsen number < 0.01. The standard atmospheric tables indicate that, below 100 km, the mean free path of particles is around 0.1 m. The traditional definition of the Knudsen formula evaluates to a value on the order of 2.5e-3, below the continuum flow limit. Based on the Reynold's number relation and the specific heat ratio found for the simulations that we have performed, the Knudsen number evaluates to around 3.4e-4, also below the continuum flow limit. This assures us that the use of the inviscid Euler equations used in the SPH solver is appropriate.

A.2. Calculation of bow shock geometry

The simulated Mach contour lines for the 2D circular model shock standoff cases are shown in Fig. A.1. We utilize a curve fitting algorithm via the MATLAB curve fitting toolbox along the Mach-10 contour line. As previously described, we apply a fourth order fit to the data in accordance with common practices used in the literature (Battarbee et al., 2020; Jennis et al., 2025) for bow shock geometry curve fitting techniques. The Mach contour value was selected based upon some element of trial and error, with the assumption that the value should exist somewhere between 1 and the freestream value. The intention is to find the section between the freestream condition and the post-shock subsonic region which suitably defines the shock boundary. Since this a resolution study, the thickness of that section of interest will only ever approach the realistic limit. A curve fit for the sonic, Mach = 1, contour would fail since it envelops the elliptical post-shock region near the leading edge. Curve fits for values of Mach = 2, 3, 4, and 5 resulted in the tails of the polynomial curve failing to accurately capture the oblique angle of the bow shock. At a value of Mach = 10, the fitted curve not only captures the curvature and oblique angle of the geometry adequately but, at increasing resolutions, it is consistently near the converging shock boundary, as shown in Fig. A.2.

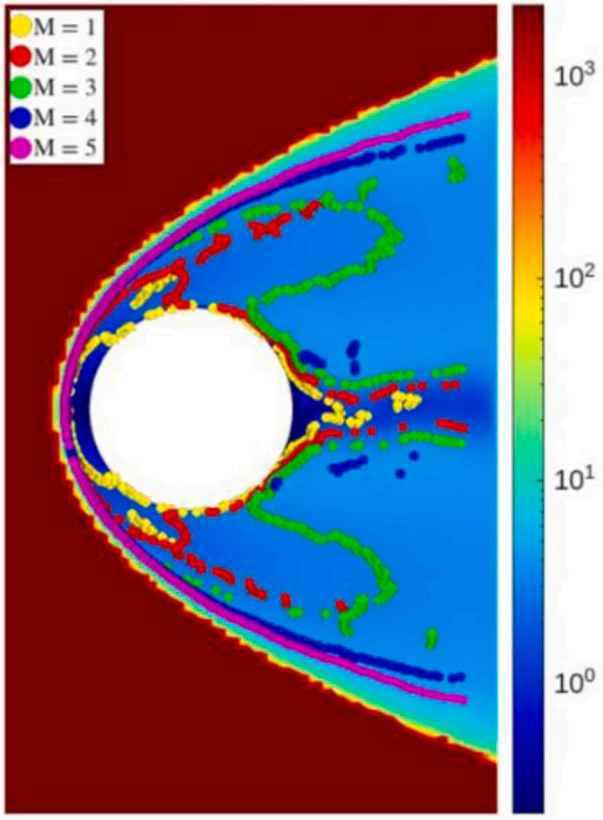

Fig. A.1. Contours of Mach = 1,2,3,4, and 5 overlaid onto the Mach field for the 60 nodes-per-radius resolution study. Mach = 1,2, and 3 fail to adequately capture the hyperbolic tail of the bow shock curve. Mach = 4 and 5 fail to capture the oblique angle of the shock. The color grade scale represents Mach number.

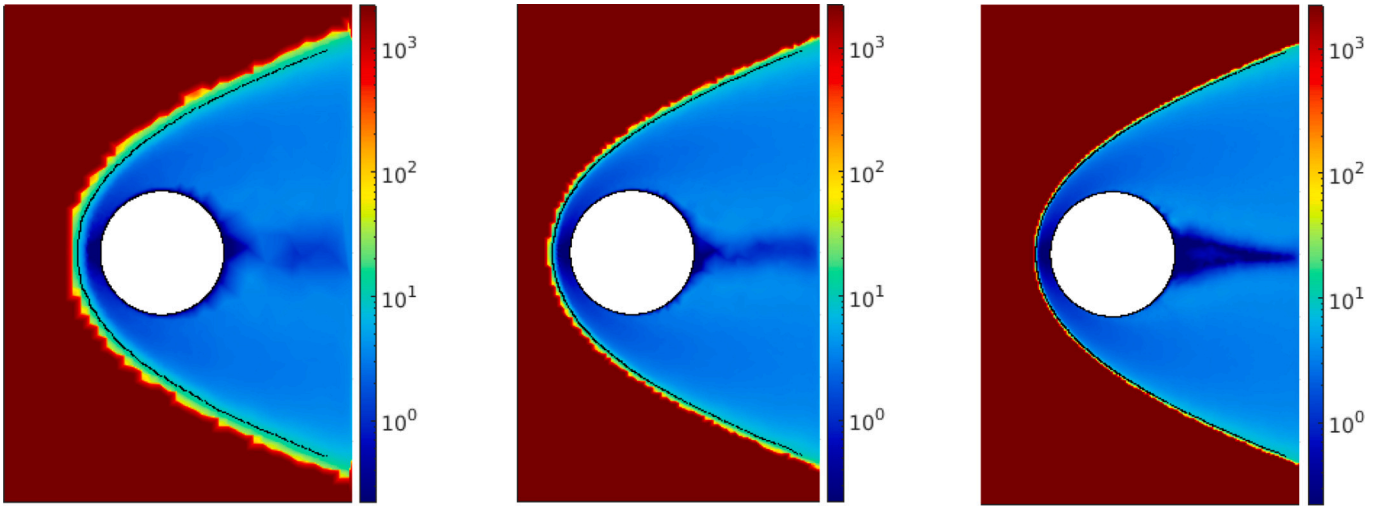

Fig. A.2. Contours of the Mach 10 line for the nodes-per-radius cases of 30, 60, and 120 respectively. The Mach = 10 contour adequately captures the shock boundary as the simulations approach convergence. The color grade scale represents Mach number.

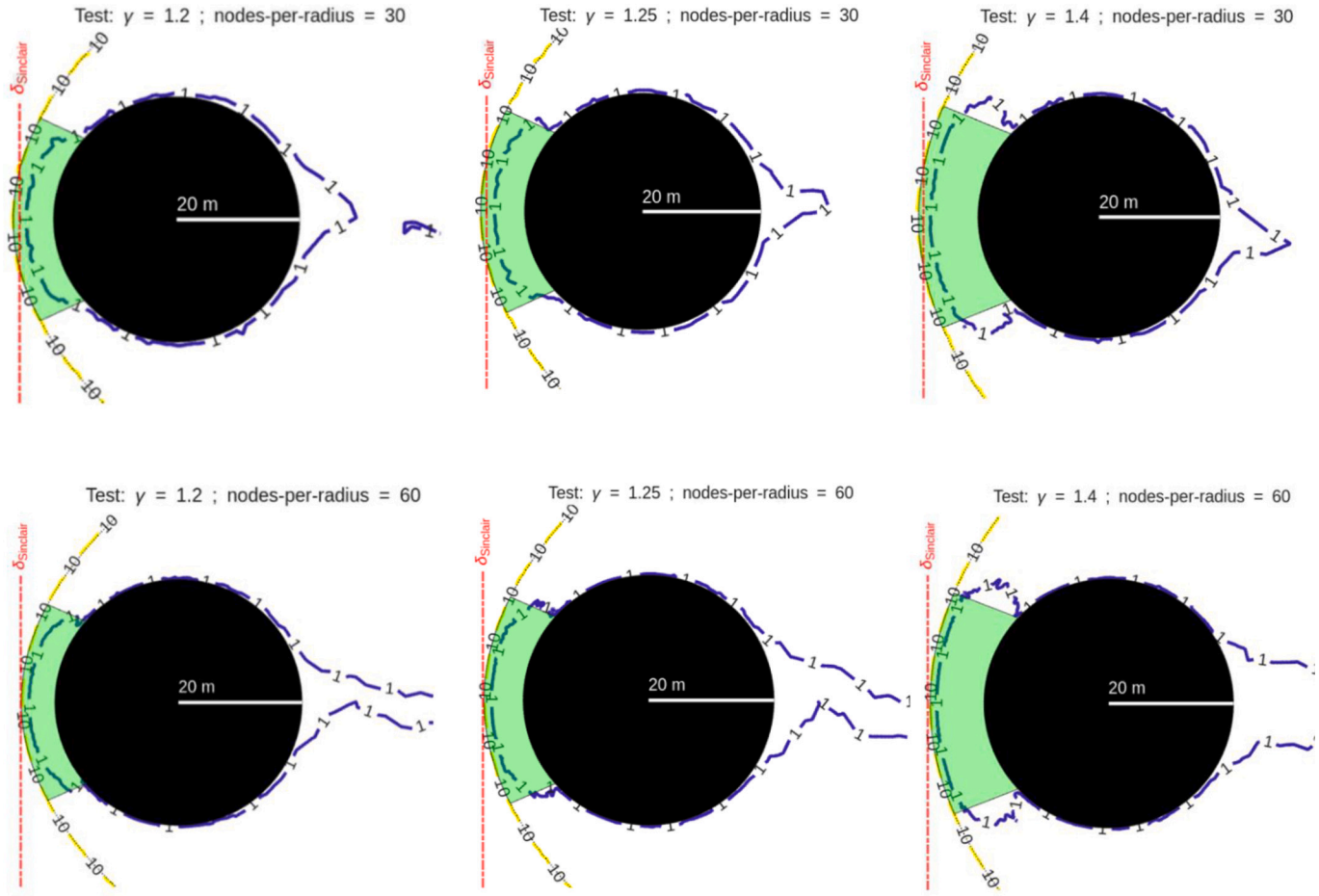

Fig. A.3. Visualizations of the Mach contour fields for Mach = 1 and 10, the fourth-order polynomial curve fit to the Mach-10 contour, the theoretical standoff distance based on eq. 32 from Sinclair and Cui (2017). (Left) Gamma-law gas with $\gamma = 1.2$ parameterized by (top) 30 and (bottom) 60 nodes-per-radius. (Center) Gamma-law gas with $\gamma = 1.25$ and (Right) gamma-law gas with $\gamma = 1.4$.

Fig. A.3. presents similar data to Fig. 7. Specifically, Fig. A.3. visualizes the bow shock geometry at increasing resolutions for the gamma-law gas cases of 1.2, 1.25, and 1.4. Notably, we include the theoretical standoff distance derived from Sinclair and Cui, 2017 as a vertical red line on the figures to demonstrate convergence of the simulated bow shock, as represented by the Mach-10 contour line.

4.1.1. Real-gas analogous specific heat ratio additional results

For the evaluated property values, the arctangent fit is applied to the LEOS based simulations at increasing resolution. With increasing resolution, the solution convergences towards a steeper slope representative of a classical step function. The difference between 60 and 120 nodes-per-radius is

relatively modest, which suggests 60 nodes-per-radius is sufficient to achieve resolution independence.

Likewise, the same evaluation is performed for the gamma-law gas cases where $\gamma = 1.2$, 1.25, and 1.4 at 30 and 60 nodes-per-radius. Note the change in the discontinuity slope between the two resolution cases; higher resolutions are representative of an approach towards convergence since the modeled shock thickness begins to 'shrink.' Comparison between the results for the LEOS cases and the gamma-law cases highlights the property value discrepancies that arise when using the ideal gas assumption with $\gamma = 1.4$.

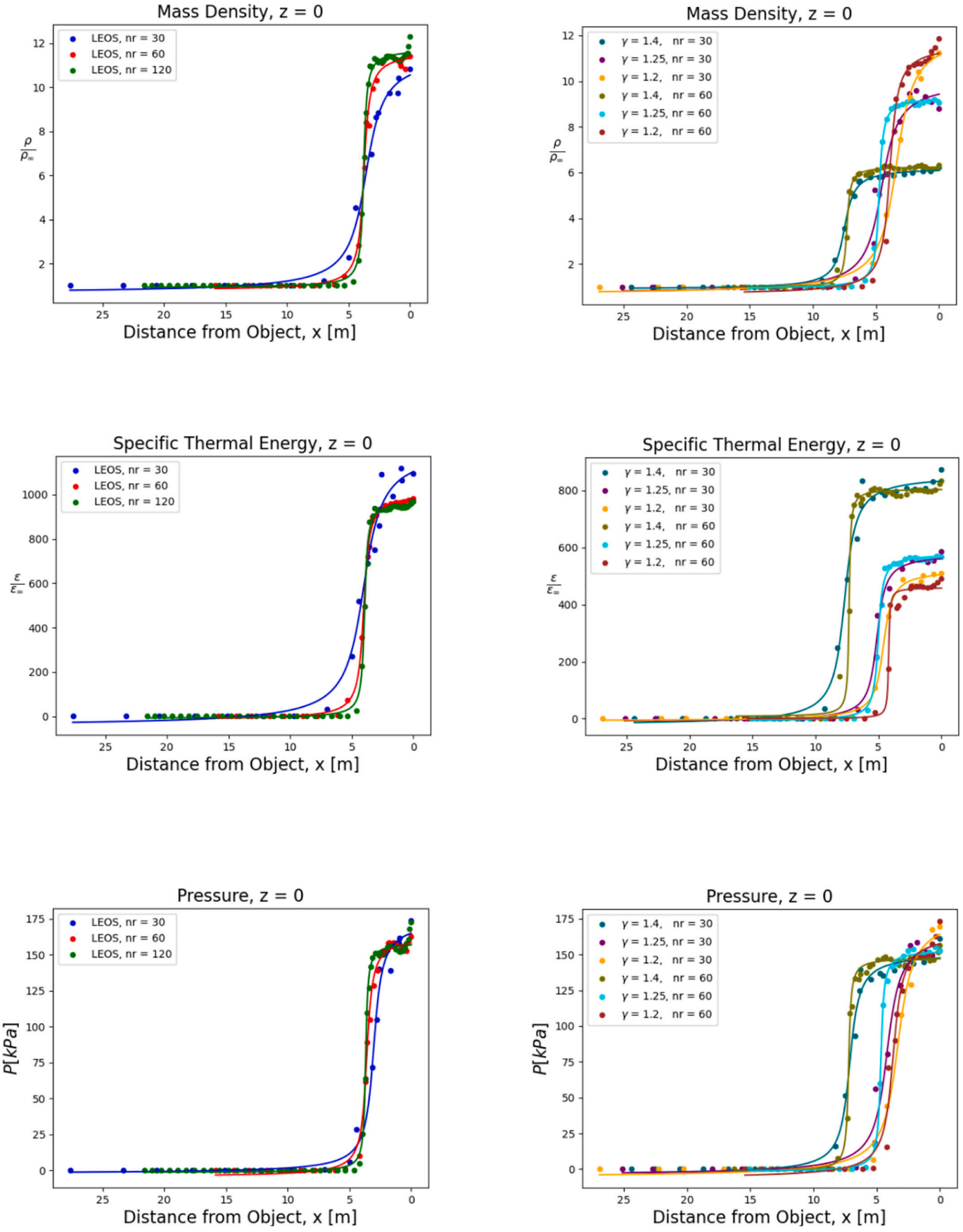

Fig. A.4. (Left) LEOS modeled cases at 30, 60, and 120 nodes spanning the circular radius and (Right) specific heat ratios of 1.2, 1.25, and 1.4 at 30 and 60 nodes spanning the circular radius. Values taken across the shock, along the stagnation line are (Top) Mass density values normalized by the freestream density (Middle)

Specific thermal energy normalized by the freestream specific thermal energy (Bottom) Pressure.

4.1.2. Flow-structure interactions – 3D spherical model additional results

Presented here are the simulated lateral and axial velocity curves for cases 9a – 9e as they relate the Laurence et al. (2012) experiments. We display the curves in both scenarios where a vertical impulse due to floss tearing is applied (lateral impulse) or not applied (no impulse). The largest effect the inclusion of the impulse force, which is modeled as a starting velocity for the respective spherical body, is a vertical displacement of the lateral velocity curve, which is more pronounced for cases 9a and 9b.

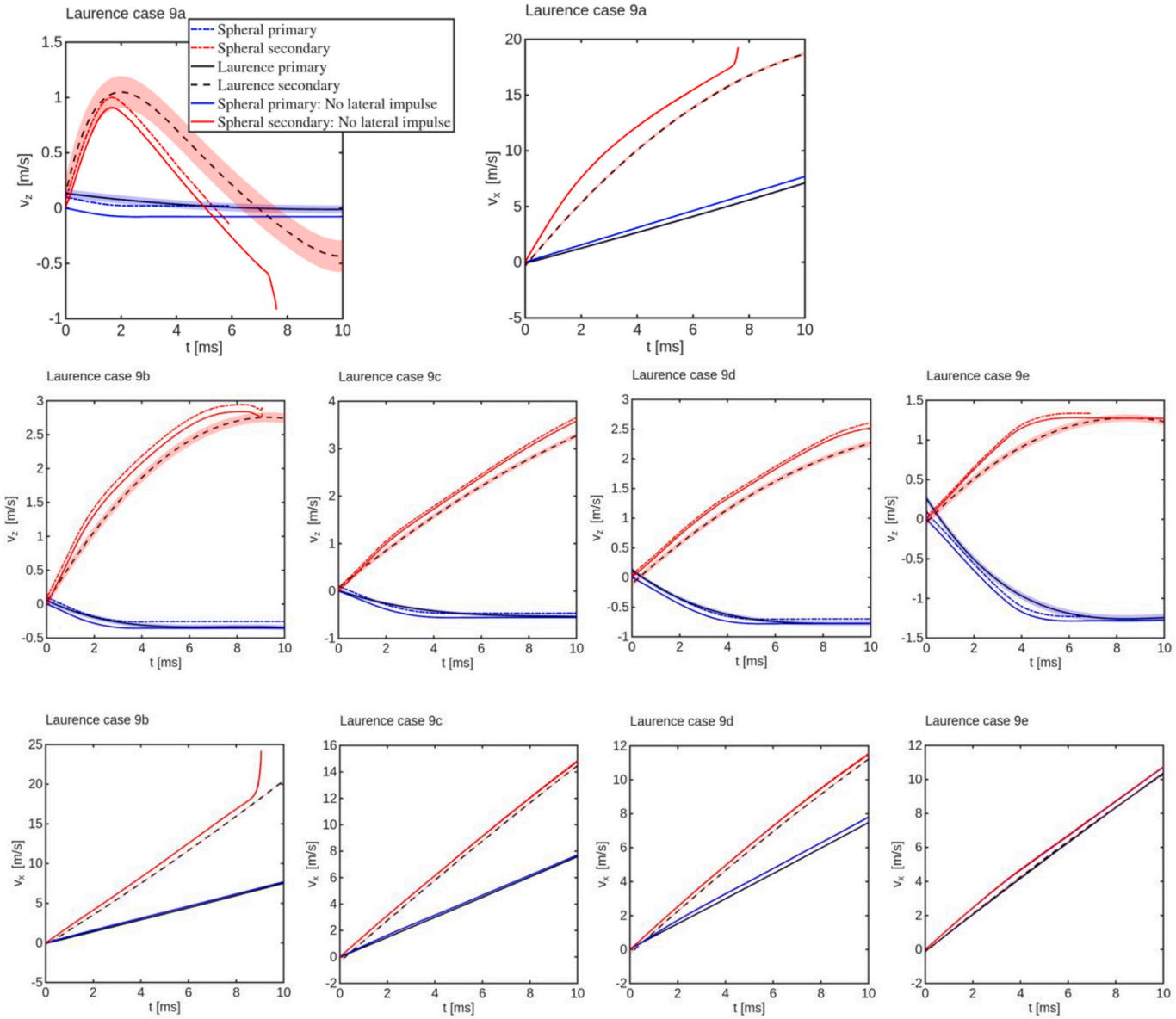

Fig. A.4. The lateral and axial velocities of the two spheres relative to their starting positions, representative of their respective Laurence et al. (2012) experimental testcases for varying spherical ratios. Includes lateral starting velocities applied and no lateral starting velocities. The top row represents case 9a ($\frac{r_2}{r_1} = 0.25$). The bottom two rows represent cases 9b ($\frac{r_2}{r_1} = 0.5$), 9c (0.625), 9d (0.75), and 9e (1).

Data availability

The data will be made available upon reasonable request. The code Spheral is publicly available on github.

References

Anderson, J.D., 2006. Hypersonic and High-Temperature Gas Dynamics, 2nd edition. American Institute of Aeronautics and Astronautics.

Artemieva, N.A., Shuvalov, V.V., 2016. From Tunguska to Chelyabinsk via Jupiter. Annu. Rev. Earth Planet. Sci. 44, 37–56.

Atherton, T.J., Kerbyson, D.J., 1999. Size invariant circle detection. Image Vis. Comput. 17, 795–803.

Avramenko, M.I., Glazyrin, I.V., Ionov, G.V., Karpeev, A.V., 2014. Simulation of the airwave caused by the Chelyabinsk superbolide. J. Geophys. Res. Atmos. 119, 7035–7050.

Battarbee, M., Ganse, U., Pfau-Kempf, Y., Turc, L., Brito, T., Grandin, M., Koskela, T., Palmroth, M., 2020. Non-locality of earth's quasi-parallel bow shock: injection of thermal protons in a hybrid-Vlasov simulation. Ann. Geophys. 35 (3), 625–643.

Bedarov, I.A., Fedorov, A.V., Fomin, V.M., 2011. Numerical analysis of the flow around a system of bodies behind the shock wave. Combust. Explos. Shock Waves 48 (4), 446–454.

Billig, F.S., 1967. Shock-wave shapes around spherical and cylindrical-nosed bodies. J. Spacecr. Rocket. 4 (6), 822–823.

Borovicka, J., 2015. The Chelyabinsk event. Proceedings of the International Astronomical Union 11 (A29A), 247–252.

Borovicka, J., Spurny, P., Brown, P., Wiegert, P., Kalenda, P., Clark, D., Shrbeny, L., 2013. The trajectory, structure and origin of the Chelyabinsk asteroidal impactor. Nature 503, 235–237.
Boslough, M.B.E., Crawford, D.A., 1997. Shoemaker-levy 9 and plume-forming collisions on earth. Ann. N. Y. Acad. Sci. 822, 236–282.
Boslough, M.B.E., Crawford, D.A., 2008. Low-altitude airbursts and the impact threat. Int. J. Impact Eng. 35 (12), 1441–1448.
Boslough, M., Brown, P.G., Clark, D., Wiegert, P., Ye, Q., 2026. 2032 and 2036 risk enhancement from NEOs in the Taurid stream: is there a significant coherent component to impact risk? Acta Astronaut. 238 (B), 710–715.
Brown, P., Spalding, R.E., ReVelle, D.O., Tagliaferri, E., Worden, S.P., 2002. The flux of small near-earth objects colliding with the earth. Nature 420, 294–296.
Brown, P.G., Assink, J.D., Astiz, L., Blaauw, R., Boslough, M.B., Borovicka, J., Brachet, N., Brown, D., Campbell-Brown, M., Ceranna, L., Cooke, W., de Groot-Hedlin, C., Prob, D.P., Edwards, W., Evers, L.G., Garces, M., Gill, J., Hedlin, M., Kingery, A., Laske, G., Le Pichon, A., Mialle, P., Moser, D.E., Saffer, A., Silber, E., Smets, P., Spalding, R.E., Spurny, P., Tagliaferri, E., Uren, D., Weryk, R.J., Whitaker, R., Krzeminski, Z., 2013. A 500-kiloton airburst over Chelyabinsk and an enhanced hazard from small impactors. Nature 503, 238–241.
Campbell-Brown, M.D., Koschny, D., 2004. Model of the ablation of faint meteors. Astron. Astrophys. 418, 751–758.
Cardona, V., Lago, V., 2023. Investigation of shock/shock interferences on the aerodynamics of a fragment in the wake of a debris in a rarefied regime/at high altitude. J. Fluid Mech. 973, A26.
Ceplecha, Z., Revelle, D.O., 2010. Fragmentation model of meteorid motion, mass loss, and radiation in the atmosphere. Meteorit. Planet. Sci. 40 (1), 35–54.
Chyba, C.F., Thomas, P.J., Zahnle, K.J., 1993. The 1908 Tunguska explosion: atmospheric disruption of a stony asteroid. Nature 361, 40–44.
Emelyanenko, V.V., Popova, O.P., Chugai, N.N., Shelyakov, M.A., Pakhomov, Y.V., Shustov, B.M., Shuvalov, V.V., Biryukov, E.E., Rybnov, Y.S., Marov, M.Y., Rykhlova, L.V., Naroenkov, S.A., Kasrtashova, A.P., Kharlamov, V.A., Trubetskaya, I. A., 2013. Astronomical and physical aspects of the Chelyabinsk event. Sol. Syst. Res. 47 (4), 240–254.
Emel'yanenko, V.V., Naroenkov, S.A., Jenniskens, P., Popova, O.P., 2014. The orbit and dynamical evolution of the Chelyabinsk object. Meteorit. Planet. Sci. 49, 2169–2174.
Fritsch, F.N., 2016. LIP: The Livermore Interpolation Package, Version 1.6. Report. Lawrence Livermore National Laboratory.
Frontiere, N., Raskin, C., Owen, J., 2017. CRKSPH – A conservative reproducing kernel smoothed particle hydrodynamics scheme. J. Comput. Phys. 332, 160–209. https://doi.org/10.1016/j.jcp.2016.12.004.
Gamgami, F., Sinnhuber, M., Palm, M., von Savigny, C., 2009. In-situ exploration of earth's atmosphere using novel spacecraft design. In: 60th International Astronautical Congress 2009, 2009. IAC, p. 3.
Harris, A.W., Chodas, P.W., 2021. The population of near-Earth asteroids revisited and updated. Icarus 365.
Hills, J.G., Goda, M.P., 1993. The fragmentation of small asteroids in the atmosphere. Astron. J. 105 (3), 1114–1144.
Jennis, E., Jones, L., Williams, O., 2025. Thermodynamic scaling of supersonic retropropulsion flowfields. Exp. Fluids vol 66 (38).
Jenniskens, P., Popova, O.P., Glazachev, D.O., Podobnaya, E.D., Kartashova, A.P., 2019. Tunguska eyewitness accounts, injuries, and casualties. Icarus 327, 4–18.
Kansa, E.J., 1988. Shock computations with adaptive mesh refinement and moving grids. Comput. Math. Applic. 15 (6–8), 623–634.
Kline, S.J., McClintock, F.A., 1953. Describing uncertainties in single-sample experiments. Mech. Eng. 75 (1), 3–8.
Kulik, L., 1936. Preliminary results of the meteorite expeditions made in the decade 1921-31. Translated by L. La Paz and G. Weins. Meteor. Planet. Sci. 2 (2), 15–20.
Laurence, S.J., Deiterding, R., 2011. Shock-wave surfing. J. Fluid Mech. 676, 396–431.
Laurence, S.J., Karl, S., 2010. An improved visualization-based force-measurement technique for short-duration hypersonic facilities. Exp. Fluids 48 (6), 949–965.
Laurence, S.J., Deiterding, R., Hornung, G., 2007. Proximal bodies in hypersonic flow. J. Fluid Mech. 590, 209–237.
Laurence, S.J., Parziale, N.J., Deiterding, R., 2012. Dynamical separation of spherical bodies in supersonic flow. J. Fluid Mech. 713, 159–182.
Longo, G., 2007. Comet/asteroid impacts and human society: Tunguska event. Springer 303–330.
Lovering, J., Parry, L., Jaeger, J., 1960. Temperatures and mass losses in iron meteorites during ablation in the earth's atmosphere. Geochim. Cosmochim. Acta 19 (3), 156–157.
Mathias, D.L., Wheeler, L.F., Dotson, J.L., 2017. A probabilistic asteroid impact risk model: assessment of sub-300 m impacts. Icarus 289, 106–119.
Moss, J.N., Bird, G.A., 1984. Direct simulation of transitional flow for hypersonic reentry conditions. In: AIAA 22nd Aerospace Sciences Meeting.
Mouton, C.A., Hornung, H.G., 2008. Experiments on the mechanism of inducing transition between regular and Mach reflection. Phys. Fluids 20, 126103.
NASA, 1976. US standard atmosphere 1976. In: NASA-TM-X-74335. Government Printing Office, U.S.
Noh, W., 1987. Errors for calculations of strong shocks using an artificial viscosity and an artificial heat flux. J. Comput. Phys. 72, 78–120.
Opik, E.J., 1958. Physics of Meteor Flight in the Atmosphere. Dover.
Owen, J.M., 2010. ASPH Modeling of Material Damage and Failure. USDOE.
Owen, J.M., Villumsen, J.V., Shapiro, P.R., Martel, H., 1998. Adaptive smoothed particle hydrodynamics: methodology 2. Astrophys. J. 116 (2), 155–209.
Passey, Q.R., Melosh, H.J., 1980. Effects of atmospheric breakup on crater field formation. Icarus 42, 211–233.
Pearl, J.M., Raskin, C.D., Owen, J.M., 2022. FSISPH: an SPH formulation for impacts between dissimilar materials. J. Comput. Phys. 469, 111533.
Pearl, J.M., Raskin, C.D., Owen, J.M., Kumamoto, K.M., Syal, M.B., 2023. Insights into the failure mode of the Chelyabinsk meteor from high-fidelity simulation. Icarus 404, 115686.
Popova, O., 2021, January 22. Chelyabinsk Meteorite. Oxford Research Encyclopedia of Planetary Science.
Popova, O., Borovicka, J., Hartmann, W.K., Spurny, P., Gnos, E., Nemtchinov, I., Trigo-Rodriguez, J.M., 2011. Very low strengths of interplanetary meteoroids and small asteroids. Meteorit. Planet. Sci. 46, 1525–1550.
Popova, O.P., Jenniskens, P., Emelyanenko, V., Kartashova, A., Biryukov, E., Khaibrakhmanov, S., Shuvalov, V., Rybnov, Y., Dudorov, A., Grokhovsky, V.I., Badyukov, D.D., Yin, Q., Gural, P.S., Albers, J., Granvik, M., Evers, L.G., Kuiper, J., Kharlamov, V., Solovyov, A., Rusakov, Y.S., Korotkiy, S., Serdyuk, I., Korochantsev, A.V., Larionov, M.Y., Glazachev, D., Mayer, A.E., Gisler, G., Gladkovsky, S.V., Wimpenny, J., Sanborn, M.E., Yamakawa, A., Verosub, K.L., Rowland, D.J., Roeske, S., Botto, N.W., Friedrich, J.M., Zolensky, M.E., Le, L., Ross, D., Ziegler, K., Nakamura, T., Ahn, I., Lee, J.I., Zhou, Q., Li, X., Li, Q., Liu, Y., Tang, G., Hiroi, T., Sears, D., Weinstein, I.A., Vokhmintsev, A.S., Ishchenko, A.V., Schmitt-Kopplin, P., Hertkorn, N., Nagao, K., Haba, M.K., Komatsu, M., Mikouchi, T., 2013. Chelyabinsk airburst, damage assessment, meteorite recovery, and characterization. Science 342 (6162), 1069–1073.
Raghunandan, P., Haskins, J.B., Palmer, G.E., Bessire, B.K., Stern, E.C., 2022. Material response modeling of melt flow-vapor ablation for iron. AIAA J. 60 (4), 2028–2038.
Raskin, C., Owen, J., 2016. Rapid optimal SPH particle distributions in spherical geometries for creating astophysical initial conditions. Astrophys. J. 820 (2), 1–7.
Register, P.J., Mathias, D.L., Wheeler, L.F., 2017. Asteroid fragmentation approaches for modeling atmospheric energy deposition. Icarus 284, 157–166.
Register, P.J., Aftosmis, M.J., Stern, E.C., Brock, J.M., Seltner, P.M., Willems, S., Guelhan, A., Mathias, D.L., 2020. Interactions between asteroid fragments during atmospheric entry. Icarus 337.
Robertson, D.K., Mathias, D.L., 2019. Hydrocode simulations of asteroid airbursts and constraints for Tunguska. Icarus 327, 36–47.
Rulko, T.A., Rau, A., Chomette, G., Wheeler, L., Mathias, D., Dotson, J., Radovitzky, R., 2025. Stress analysis of asteroids during atmospheric entry and implications for the breakup criterion. Icarus 434 (12), 116526.
Sedov, L., 1959. Similarity & Dimensional Methods in Mechanics. Academic Press Inc.
Sembian, S., Liverts, M., Tillmark, N., Apazidis, N., 2016. Plane shock wave interaction with a cylindrical water column. Phys. Fluids 28, 056102.
Shao, M., Nemati, B., Zhai, C., Turyshev, S.G., Sandhu, J., Hallinan, G., Harding, L.K., 2014. Finding very small near-earth asteroids using synthetic tracking. Astrophys. J. 782, no. 1.
Shepard, C.E., Stine, H.A., Vorreiter, J.W., Winovich, W., 1967. A study of artificial meteors as ablators. NASA TN D-3740.
Shuvalov, V., Svetsov, V., Popoova, O., Glazachev, D., 2017. Numerical model of the Chelyabinsk meteoroid as a strengthless object. Planet. Space Sci. 147, 38–47.
Silber, E.A., Boslough, M., Hocking, W.K., Gritsevich, M., Whitaker, R.W., 2018. Physics of meteor generated shock waves in the earth's atmosphere- A review. Adv. Space Res. 62 (3), 489–532.
Sinclair, J., Cui, X., 2017. A theoretical approximation of the shock standoff distance for supersonic flows around a circular cylinder. Phys. Fluids 29, 026102.
Sod, G.A., 1978. A survey of several finite difference methods for systems of nonlinear hyperbolic conservation laws. J. Comput. Phys. 27, 1–31.
Tillotson, J.H., 1962. Metallic equations of state for hypervelocity impact. Gener. Atom. Rep. GA-3216. Technical Report.
Wheeler, L.F., Register, P.J., Mathias, D.L., 2017. A fragment-cloud model for asteroid breakup and atmospheric energy deposition. Icarus 295, 149–169.
Xiang, G., Wang, B., 2017. Numerical study of a planar shock interacting with a cylindrical water column embedded with an air cavity. J. Fluid Mech. 825, 825–852.
Zaytsev, D., Borodin, E.N., Dudorov, A.E., Panfilov, P., 2021. The mechanical properties of Chelyabinsk LL5 chondrite under compression and tension. Earth Moon Planet. 125 (2).